Journal of Sound and Vibration 495 (2021) 115905

Contents lists available at ScienceDirect

Journal of Sound and Vibration

journal homepage: www.elsevier.com/locate/jsv

Do we need non-linear corrections? On the boundary Forchheimer equation in acoustic scattering

Matthew J. Colbrook*, Lorna J. Ayton

Department of Applied Mathematics and Theoretical Physics, University of Cambridge, Wilberforce Road, CB3 0WA, UK

ARTICLE INFO

Article history:
Received 24 September 2020
Revised 23 November 2020
Accepted 7 December 2020
Available online 15 December 2020

Keywords:
Acoustic scattering
Trailing-edge noise
Porous airfoils
Spectral methods
Non-linear boundary conditions

ABSTRACT

This paper presents a rapid numerical method for predicting the aerodynamic noise generated by foam-like porous aerofoils. In such situations, particularly for high-frequency noise sources, Darcy's law may be unsuitable for describing the pressure jump across the aerofoil. Therefore, an inertial Forchheimer correction is introduced. This results in a non-linear boundary condition relating the pressure jump across the material to the fluid displacement. We aim to provide a quick, semi-analytical model that incorporates such non-linear effects without requiring a full turbulent simulation. The numerical scheme implemented is based on local Mathieu function expansions, leading to a semi-analytical boundary spectral method that is well-suited to both linear and non-linear boundary conditions (including boundary conditions more general than the Forchheimer correction). In the latter case, Newton's method is employed to solve the resulting non-linear system of equations for the unknown coefficients. Whilst the physical model is simplified to consider just the scattering by a thin porous aerofoil with no background flow, when the non-linear inertial correction is included good agreement is seen between the model predictions and both experimental results and large eddy simulations. It is found that for sufficiently low-permeability materials, the effects of inertia can outweigh the noise attenuation effects of viscosity. This helps explain the discrepancy between experimental results and previous (linear) low-fidelity numerical simulations or analytical predictions, which typically overestimate the noise reduction capabilities of porous aerofoils.

1. Introduction

The use of porosity as a means to control and attenuate aerofoil-interaction noise has become increasingly popular over recent years [1–5]. Within this notion of porosity lies two distinct concepts. The first arises for thin perforated plates [4,5], whereby apertures fully puncture the material. Here, when there is no background steady flow, the apertures induce an acoustic (Rayleigh) conductivity on the surface [6], and when there is background flow (tangential [7] or bias [8]), the vorticity generated by that flow over the apertures acts dissipatively. Both mechanisms may be captured by the Rayleigh conductivity parameter, K_R, whose real part corresponds to conductivity and whose imaginary part to dissipation. The acoustic pressure, $pe^{-i\omega t}$ (where the factor $e^{-i\omega t}$ will be suppressed throughout), on a thin plate lying in $y = 0$ must satisfy the

* Corresponding author.
E-mail addresses: m.colbrook@damtp.cam.ac.uk (M.J. Colbrook), l.j.ayton@damtp.cam.ac.uk (L.J. Ayton).

https://doi.org/10.1016/j.jsv.2020.115905
0022-460X/

condition

$$K_R[p] = \mathrm{i}\rho_f \omega v, \tag{1.1}$$

where ρ_f is the external fluid density and v is the normal fluid velocity averaged over a unit area of the surface. We use the notation $p(x, 0+)$ and $p(x, 0-)$ to denote the values of the pressure field just above and just below the plate respectively, and for notational convenience, the jump $p(x, 0+) - p(x, 0-)$ across the plate is denoted by $[p](x)$. Under Howe's derivation [7], the condition in (1.1) is valid only when the open area of the plate is sufficiently small (low porosity), and the wavenumber is much smaller than the reciprocal of a typical pore radius.

The second notion of porosity arises for materials such as metal foams [1,9], wherein microscopic void spaces are found within a rigid framework. Here, the local Reynolds number, based on typical void space (pore size) within the foam, is low and therefore viscous dissipation plays a dominant role. For sufficiently low local Reynolds numbers ($\mathrm{Re}_L < 1$), only the viscous dissipation is important, and the pressure jump across these materials may be described linearly by Darcy's Law,

$$K\frac{[p]}{h} = -\mu v,$$

where μ is the air viscosity, K is the permeability of the material and h is the small height over which the pressure jump is taken. However, at higher local Reynolds numbers ($1 < \mathrm{Re}_L < 10$), a correction for inertial effects should be included, and the pressure difference may be described by the non-linear boundary Forchheimer equation [10],

$$K\frac{[p]}{h} = -\mu v - \beta\rho_f\sqrt{K}\, v|v|, \tag{1.2}$$

where β is the inertial coefficient. Note also that the nature of this boundary condition still permits the time-harmonic form $\sim \mathrm{e}^{-\mathrm{i}\omega t}$.

Previous theoretical [5] and low-fidelity numerical [11] work concerned with the prediction of aerodynamic noise scattering and absorption by porous materials focuses on the first notion of porosity, perforated plates, as these can be easily described by two parameters; the Rayleigh conductivity, K_R, and an open area ratio, α, of the surface. Due to the complexity of a background steady flow interacting with a porous material, these models do not include such a background flow and are purely concerned with acoustic scattering. For further simplicity, the models consider the boundary conditions to be linearised to $y = 0$, thus effectively reducing an aerofoil to a flat plate. Both semi-infinite and finite plate models have been considered this way [5,11]. Experimental findings show that porosity is effective at reducing low and mid-frequency noise, both for perforations and foam-like materials [3,4]. Theoretical and low-fidelity linear numerical models can capture this feature. However, these models often *overpredict* the potential reduction of noise. Often at mid and high frequencies, the discrepancy with experimental results is attributed to surface roughness, which is generated by the background flow interacting with the rough surface and is not accounted for in the theoretical models.

Fewer models consider foam-like porous aerofoils, despite these being commonplace in the experimental literature. At high frequencies for these foam-like materials, the local Reynolds number can be sufficiently high within the material to require the inclusion of the non-linear Forchheimer correction. The Large Eddy Simulations (LES) conducted by Koh et al. [12,13], which do take account of the Forchheimer correction, corroborate the reduction of noise observed experimentally, and thus confirm that current linear models overpredict noise reduction. Accordingly, this paper investigates the effect of this non-linear inertial term on the acoustic scattering by thin porous aerofoils, and quantifies the effect of the non-linear boundary condition on noise reduction versus a linear (Darcy) model. We aim to provide a quick, semi-analytical model that incorporates the non-linear effects of the Forchheimer model without requiring a full turbulent simulation (such as the models in Bae and Moon [14], Ananthan et al. [15]).

To implement the non-linear condition, we extend a previous linear boundary collocation method [11,16,17], which represents the solution in terms of local Mathieu function expansions. In the context of the current paper, this method, along with a partitioning of the system according to the different (kinematic and non-linear Forchheimer) boundary conditions, gives rise to a non-linear system of equations (see (3.10)) for the unknown coefficients, which we solve via Newton's method. The result is a boundary spectral method that can deal with the non-linear Forchheimer correction, and more general non-linear boundary conditions, efficiently and accurately for a wide range of parameters.

This paper is organised as follows. In Section 2, we introduce the mathematical model. The numerical method is presented in Section 3, with convergence discussed in Section 4. The results for physical models are presented and discussed in Section 5, including a comparison with LES and experimental data. A conclusion and discussion of future work is given in Section 6. Finally, code for the numerical method can be found at https://github.com/MColbrook/MathieuFunctionCollocation.

2. Mathematical model

Suppose that an acoustic source interacts with a plate $\{(x, 0) : -1 \le x \le 1\}$ (where lengths have been non-dimensionalised by the semi-chord, d). The thickness of the plate, $h(x)$, which is permitted to vary in the x direction, is constrained to be much smaller than the semichord, $h(x) \ll 1$, and hence we consider the zero-thickness approximation. We illustrate the setup in Fig. 1 where a lateral quadrupole is chosen to illustrate the acoustic source. The source will have pressure denoted by p_{I} and the scattered field has pressure denoted by p. We assume that p and p_{I} have the usual time

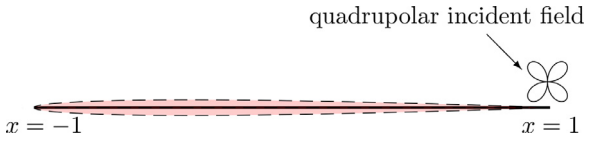

Fig. 1. Schematic of the single plate $\{(x,0):-1\le x\le 1\}$ (zero-thickness approximation) with a quadrupolar source. The shaded area corresponds to $h(x)$ of an NACA 4-digit aerofoil with 6% thickness.

dependence $\mathrm{e}^{-\mathrm{i}\omega t}$ (omitted throughout) and therefore p satisfies the Helmholtz equation

$$\left(\frac{\partial}{\partial x^2}+\frac{\partial}{\partial y^2}+k_0^2\right)p=0,$$

where $k_0=\omega/c_0$ is the acoustic wavenumber for angular frequency ω. Here, pressure has been non-dimensionalised by $\rho_f c_0^2$, where c_0 is the speed of sound.

We shall focus on two primary sources; first, the pressure due to an acoustic plane wave of unit amplitude incident at angle θ (measured from the positive x-axis anticlockwise in the usual manner), corresponding to the choice

$$p_{\mathrm{I}}(x,y)=\mathrm{e}^{-\mathrm{i}k_0x\cos\theta-\mathrm{i}k_0y\sin\theta}. \tag{2.1}$$

The second choice, most applicable to an aerodynamic setting, is a near-field quadrupole sound source corresponding to

$$p_{\mathrm{I}}(x,y)=P_0\frac{\mathrm{i}k_0^2}{4r_0^2}(x-x_0)(y-y_0)H_2^{(1)}(k_0r_0), \tag{2.2}$$

where (x_0,y_0) is the source location, $r_0(x,y)=\sqrt{(x-x_0)^2+(y-y_0)^2}$, and $H_n^{(1)}$ denotes the nth order Hankel function of the first kind. We mention, however, that an arbitrary acoustic source could just as easily be used. In an aerodynamic setting, the principle source of noise arises from quadrupole type sources, $\sim\frac{\partial T_{ij}}{\partial x_i x_j}$, as described by Lighthill [18], where $T_{ij}=\rho u_i u_j$ is the Lighthill tensor, with ρ and $u_{i,j}$ the typical (dimensional) density and (dimensional) velocities of the turbulent flow. We therefore allocate a (non-dimensionalised) scaling of the quadrupole corresponding to $P_0=M^2$, where M is the (low) Mach number of the flow local to the quadrupole.

We denote the (non-dimensionalised) average fluid displacement normal to the plate by η_a, where averaging is done over a unit area of the porous material. Therefore, the non-dimensionalised kinematic condition on the plate takes the form

$$\left.\frac{\partial p}{\partial y}\right|_{y=0}+\left.\frac{\partial p_{\mathrm{I}}}{\partial y}\right|_{y=0}=C_0(x)\eta_a|_{y=0},\qquad |x|<1, \tag{2.3}$$

with $C_0(x)=k_0^2$. Here we have neglected $O(h)$ terms arising from the small thickness of the plate allowing us to present a condition along $y=0$.

The non-linear Forchheimer condition (similarly applied on $y=0$ by taking only leading order in h) is

$$[p]=C_1(x)\eta_a+C_2(x)\eta_a|\eta_a|,\qquad |x|<1, \tag{2.4}$$

where $C_1(x)=\mathrm{i}k_0h(x)/G_{rn}$, and $C_2(x)=\mathrm{i}G_{rf}h(x)k_0^2/G_{rn}$ are defined in terms of the non-dimensional groups $G_{rn}=\rho_f K c_0/(\mu d)$, and $G_{rf}=\rho_f\beta c_0\sqrt{K}/\mu$ as in Cimolin and Discacciati [10]. (Recall that d is the dimensional semichord length.) It is important to note here that we include the non-linear term $C_2(x)\eta_a|\eta_a|$, since is not necessarily smaller than the linear term $C_1(x)\eta_a$, despite including an additional factor of η_a. Inclusion of this term is necessary when $G_{rf}k_0$ is larger than $O(1)$, which is linked both to higher frequencies and higher permeability materials. It is particularly the high-frequency regime we wish to interrogate in order to consolidate previous linear theory of noise reduction with experimental measurements.

When $|x|>1$, continuity and symmetry requires $p(x,0)=0$, and the solution p is also required to satisfy the Sommerfeld radiation condition for outgoing waves at infinity given by

$$\lim_{r\to\infty}r^{-1/2}\left(\frac{\partial p}{\partial r}-\mathrm{i}k_0p\right)=0,\qquad \text{where } r=\sqrt{x^2+y^2}.$$

Finally, we have written the boundary conditions (2.3) and (2.4) in a general form with coefficients $C_{0,1,2}$, since the collocation method can deal with this generality. However, our focus will be on the above specified values of C_i throughout. Additionally, the method can be extended to different non-linear couplings in (2.4), for example, sums of terms involving $\eta_a|\eta_a|^\alpha$ for $\alpha>-1$ or higher-order corrections.

3. Numerical method of solution

We first consider the case of a single plate, where we compute the solution using separation of variables following the method outlined in Ayton et al. [11], Colbrook and Priddin [16], Colbrook and Kisil [17]. This induces the well-known

expansion of the pressure field in terms of Mathieu functions, initially with unknown coefficients that must be determined by the boundary conditions (see the discussions and references in the above papers for the history of earlier methods that use Mathieu functions, such as the early work of Morse and Rubenstein [19] or the recent boundary integral method of Nigro [20], discussed also in Colbrook et al. [21], Ayton et al. [22], for a single rigid impermeable plate). Additionally, we expand η_a in Chebyshev polynomials (of the first kind). To cope with the resulting non-linear system of equations that determine the coefficients in these expansions (as opposed to the linear systems of equations appearing in Colbrook and Priddin [16], Colbrook and Kisil [17]), we collocate and use Newton's method. Through a local separation of variables, we can also handle multiple plates, as outlined in Section 3.3 and demonstrated in Section 4.2, though this is not the focus of the current study.

3.1. The single plate case and Mathieu functions

For a plate $\{(x,0) : -d \le x \le d\}$, the scattered field p is an odd function in the variable y and hence we can consider solving the PDE system in the upper-half plane $\{(x,y) : y > 0\}$. We introduce elliptic coordinates via $x = d\cosh(\nu)\cos(\tau), y = d\sinh(\nu)\sin(\tau)$, where, with an abuse of notation, we write functions of (x,y) also as functions of (ν,τ). Under this transformation, the appropriate domain becomes $\nu \ge 0$ and $\tau \in [0,\pi]$. To simplify the formulae, we let $Q = d^2k_0^2/4$. Separation of variables leads to the expansion

$$p(\nu,\tau) = \sum_{m=1}^{\infty} a_m \mathrm{se}_m(\tau)\mathrm{Hse}_m(\nu), \tag{3.1}$$

where $\mathrm{se}_m(\tau) = \mathrm{se}_m(Q;\tau)$ denote sine-elliptic functions and $\mathrm{Hse}_m(Q;\nu) = \mathrm{Hse}_m(\nu)$ denote Mathieu–Hankel functions. Full details of this process can be found in, for example, Colbrook and Priddin [16], Colbrook and Kisil [17], Colbrook et al. [21].

We expand the functions se_m in a sine series given by

$$\mathrm{se}_m(\tau) = \sum_{l=1}^{\infty} B_l^{(m)} \sin(l\tau), \tag{3.2}$$

where we find the coefficients $B_l^{(m)}$ via a simple Galerkin method. The functions $\mathrm{Hse}_m(\nu)$ can be expanded using Bessel functions [23,24]:

$$\mathrm{Hse}_m(\nu) = \sum_{l=1}^{\infty} \frac{(-1)^{l+m}B_l^{(m)}}{\hat{C}_m} \left[J_{l-1}\left(\mathrm{e}^{-\nu}\sqrt{Q}\right)H_{l+p_m}^{(1)}\left(\mathrm{e}^{\nu}\sqrt{Q}\right) - J_{l+p_m}\left(\mathrm{e}^{-\nu}\sqrt{Q}\right)H_{l-1}^{(1)}\left(\mathrm{e}^{\nu}\sqrt{Q}\right)\right], \tag{3.3}$$

where $p_m = 1$ if m is even and $p_m = 0$ if m is odd. Here J_n denotes the Bessel function of the first kind of order n and we remind the reader that $H_n^{(1)}$ denotes the Hankel function of the first kind of order n. We choose the normalisation constants $\hat{C}_m$ such that $\mathrm{Hse}_m'(0) = 1$. In certain parameter regimes, some care must be applied when using (3.3); see [17] for details on using asymptotic expansions to avoid underflow and overflow associated with cancellations between the Bessel and Hankel functions.

We use the boundary conditions to solve for the unknown coefficients a_m, after which the solution can be evaluated anywhere in the (x,y) plane. Of particular interest is the far-field directivity, $D(\theta)$, which is defined via

$$p(r,\theta) \sim D(\theta)\frac{\mathrm{e}^{\mathrm{i}wr}}{\sqrt{r}}, \quad \text{as} \quad r \to \infty,$$

where (r,θ) are the usual polar coordinates. Given the Bessel function expansion of $\mathrm{Hse}_m(\nu)$ in (3.3), we can directly compute $D(\theta)$ from (3.1) using asymptotics of Bessel functions to obtain

$$D(\theta) = \sqrt{\frac{2}{\pi k_0}} \sum_{m=1}^{\infty} \frac{a_m B_1^{(m)}}{C_m} \exp\left(\frac{(2p_m-3)\pi}{4}\mathrm{i}\right)\mathrm{se}_m(\theta).$$

An advantage of our approach is that we implicitly compute a sine series for the far-field directivity $D(\theta)$ through the expansions of the sine-elliptic functions $\mathrm{se}_m(\theta)$ given by (3.2). This allows easy computation of the scattered far-field sound, defined as

$$P = 10\log_{10}\left(\int_0^{2\pi} |D(\theta)|^2 d\theta\right), \tag{3.4}$$

and measured in dB.

3.2. Collocating the boundary conditions

We adopt a spectral collocation approach to finding the unknown coefficients in the expansion (3.1). Throughout, we denote the approximate coefficients by $\tilde{a}_m$. We truncate the expansion (3.1) to M terms and supplement the expansion of p

with an expansion of η_a in terms of Chebyshev polynomials of the first kind

$$\eta_a(x) = \sum_{j=0}^{\infty} b_j T_j\left(\frac{x}{d}\right).$$

We truncate this expansion to N terms for approximate coefficients $\tilde{b}_j$. The kinematic relation (2.3) becomes

$$\sqrt{d^2-x^2}\cdot\frac{\partial p_1}{\partial y}(x) + \sum_{m=1}^{M}\tilde{a}_m \mathrm{se}_m\left(\cos^{-1}\left(\frac{x}{d}\right)\right) = \sqrt{d^2-x^2}\cdot C_0(x)\sum_{j=0}^{N-1}\tilde{b}_j T_j\left(\frac{x}{d}\right). \tag{3.5}$$

We collocate the kinematic condition (3.5) at the points

$$\left\{d\cos\left(\frac{2j-1}{2M}\pi\right) : j=1,\dots,M\right\},$$

which correspond to (rescaled) Chebyshev points in Cartesian coordinates and equally spaced points in elliptic coordinates [25,26]. The non-linear coupling (2.4) yields

$$2\sum_{m=1}^{M}\tilde{a}_m \mathrm{se}_m\left(\cos^{-1}\left(\tfrac{x}{d}\right)\right)\mathrm{Hse}_m(0) = \left[C_1(x)+C_2(x)\left|\sum_{j=0}^{N-1}\tilde{b}_j T_j\left(\tfrac{x}{d}\right)\right|\right]\left[\sum_{j=0}^{N-1}\tilde{b}_j T_j\left(\tfrac{x}{d}\right)\right], \tag{3.6}$$

which we collocate at N Chebyshev points.

Coupling the two collocated relations, namely (3.5) and (3.6), leads to the non-linear equation

$$A\mathbf{v} + (B\mathbf{v})\circ|C\mathbf{v}| = \mathbf{c}, \tag{3.7}$$

where $A, B, C \in \mathbb{C}^{(M+N)\times(M+N)}$, $\mathbf{v}$ is the concatenated vector of the unknown coefficients $\{\tilde{a}_m, \tilde{b}_j : m=1,\dots,M, j=0,\dots,N-1\}$, $\mathbf{c}$ denotes the forcing that arises from the $\partial_y p_1$ term in (3.5), $\circ$ denotes component-wise multiplication of vectors, and the absolute value is taken component-wise. Before describing the method to numerically solve (3.7), we briefly discuss extensions to multiple plates.

3.3. Extensions to multiple plates

We can easily extend the method to scattering from multiple plates, each of which satisfies corresponding kinematic and porous boundary conditions. Suppose that we have plates $P_{[i]}$ for $i=1,\dots,S$, whose lengths are $2d_{[i]}$ (see, for example the setup shown in Section 4.2). We also suppose that the open set $\mathbb{R}^2\backslash(\cup_{i=1}^{S}P_{[i]})$ is connected (in particular, we exclude the possibility that plates enclose a region, though this can be dealt with via suitable modifications). We use sub/superscripts $[i]$ to denote quantities associated with the plate $P_{[i]}$. Each plate $P_{[i]}$ induces a corresponding scattered field given by

$$p_{[i]}(x,y) = \sum_{m=1}^{\infty} a_m^{[i]}\mathrm{se}_m\left(Q_{[i]};\tau_{[i]}\right)\mathrm{Hse}_m\left(Q_{[i]};\nu_{[i]}\right),$$

where $(\nu_{[i]},\tau_{[i]}) = (\nu_{[i]}(x,y),\tau_{[i]}(x,y))$ are elliptic coordinates centred around $P_{[i]}$, and $Q_{[i]} = d_{[i]}^2k_0^2/4$. The total scattered field is given by the sum of these contributions $p=\sum_{i=1}^{S}p_{[i]}$ and along each plate we apply kinematic conditions and non-linear coupling as before.

We take $M_{[i]}$ Mathieu functions for the expansion along the ith plate and we supplement the expansion of $p_{[i]}$ with an expansion of $\eta_a^{[i]}$ in terms of $N_{[i]}$ Chebyshev polynomials of the first kind along the plate $P_{[i]}$. The kinematic relation becomes

$$\begin{aligned}&\textstyle\sum_{m=1}^{M_i}\tilde{a}_m^{[i]}\mathrm{se}_m\left(Q_{[i]};\cos^{-1}\left(\frac{x_{[i]}}{d_{[i]}}\right)\right) - \sqrt{d_{[i]}^2-x_{[i]}^2}\cdot C_0^{[i]}(x_{[i]})\sum_{j=0}^{N_{[i]}-1}\tilde{b}_j^{[i]}T_j\left(\frac{x_{[i]}}{d_{[i]}}\right)\\ &= -\sqrt{d_{[i]}^2-x_{[i]}^2}\cdot\frac{\partial}{\partial y}\left[p_1+\sum_{j\neq i}\sum_{m=1}^{M_{[j]}}a_m^{[j]}\mathrm{se}_m\left(Q_{[j]};\tau_{[j]}\right)\mathrm{Hse}_m\left(Q_{[j]};\nu_{[j]}\right)\right](x,y),\end{aligned}$$

where $x_{[i]}$ denotes a unit speed parametrisation of the plate $P_{[i]}$ for $x_{[i]}\in[-d_{[i]},d_{[i]}]$. We collocate this relation for (x,y) points corresponding to $M_{[i]}$ Chebyshev points along $P_{[i]}$ (so that $x_{[i]}/d_{[i]}$ correspond to standard Chebyshev points). The non-linear coupling becomes

$$\begin{aligned}&2\textstyle\sum_{m=1}^{M_{[i]}}\tilde{a}_m^{[i]}\mathrm{se}_m\left(Q_{[i]};\cos^{-1}\left(\frac{x_{[i]}}{d_{[i]}}\right)\right)\mathrm{Hse}_m(Q_{[i]};0)\\ &-\left[C_1^{[i]}(x_{[i]})+C_2^{[i]}(x_{[i]})\left|\sum_{j=0}^{N_{[i]}-1}\tilde{b}_j^{[i]}T_j\left(\frac{x_{[i]}}{d_{[i]}}\right)\right|\right]\left[\sum_{j=0}^{N_{[i]}-1}\tilde{b}_j^{[i]}T_j\left(\frac{x_{[i]}}{d_{[i]}}\right)\right]=0,\end{aligned}$$

and we collocate at $N_{[i]}$ Chebyshev points along $P_{[i]}$.

Coupling the two collocated relations across all S plates, leads to a system of the form

$$A\mathbf{v} + (B\mathbf{v})\circ|C\mathbf{v}| = \mathbf{c}, \tag{3.8}$$

where now $A,B,C\in\mathbb{C}^{(\sum_{i=1}^{S}M_{[i]}+N_{[i]})\times(\sum_{i=1}^{S}M_{[i]}+N_{[i]})}$, $\mathbf{v}$ is the concatenated vector of the unknown coefficients $\{\tilde{a}_m^{[i]},\tilde{b}_j^{[i]} : m=1,\dots,M_{[i]}, j=0,\dots,N_{[i]}-1, i=1,\dots,S\}$ and $\mathbf{c}$ denotes the relevant (known) forcing term.

3.4. Solving the non-linear system

For ease of exposition, in the case of multiple plates, we set $M = \sum_{i=1}^{S} M_{[i]}$ and $N = \sum_{i=1}^{S} N_{[i]}$. To solve the discretised Eq. (3.8), we apply Newton's method, and hence it is advantageous to reduce the dimension of the non-linear system (solved at each step) as much as possible. A closer inspection of the collocation relations yields the following block structure. If we partition the unknown coefficients into first the M unknown coefficients $\{\tilde{a}_m^{[i]}\}$ and then the N unknown coefficients $\{\tilde{b}_j^{[i]}\}$, and the collocation points into the kinematic conditions and then the non-linear couplings, we obtain the following block structure of the matrices A, B and C, and the vectors $\mathbf{v}$ and $\mathbf{c}$:

$$A = \begin{pmatrix} A_{11} & A_{12} \\ A_{21} & A_{22} \end{pmatrix}, B = \begin{pmatrix} 0 & 0 \\ 0 & B_{22} \end{pmatrix}, C = \begin{pmatrix} 0 & 0 \\ 0 & C_{22} \end{pmatrix}, \mathbf{v} = \begin{pmatrix} \mathbf{v}_1 \\ \mathbf{v}_2 \end{pmatrix}, \mathbf{c} = \begin{pmatrix} \mathbf{c}_1 \\ \mathbf{0} \end{pmatrix}.$$

By considering the rows corresponding to collocating the kinematic condition, this yields the relation

$$\mathbf{v}_1 = A_{11}^{-1}(\mathbf{c}_1 - A_{12}\mathbf{v}_2). \tag{3.9}$$

Substituting this into the non-linear coupling yields

$$\left[A_{22} - A_{21}A_{11}^{-1}A_{12}\right]\mathbf{v}_2 + (B_{22}\mathbf{v}_2) \circ |C_{22}\mathbf{v}_2| = -A_{21}A_{11}^{-1}\mathbf{c}_1. \tag{3.10}$$

We solve (3.10) via Newton's method. To do this we split vectors into real and imaginary parts so that taking absolute values is differentiable almost everywhere. We also choose the linearised solution (obtained by setting $B_{22} = 0$) as our initial vector. Other choices are possible, such as a zero-padded solution vector to the non-linear equation for smaller M and N, but we stick to this choice throughout for simplicity.[1] Once $\mathbf{v}_2$ is computed, $\mathbf{v}_1$ is computed via (3.9). Note that using the decompositions reduces the dimensions of the linear systems we solve at each iteration of Newton's method from $(2M + 2N) \times (2M + 2N)$ to $(2N) \times (2N)$ (the factors of two arise from splitting into real and imaginary parts). Since the linear systems are dense, for the choice of $M = N$, and ignoring the difference in the number of iterations of Newton's method, this leads to a roughly eightfold speed-up for large $M = N$.

4. Numerical convergence

In this section, we interrogate our numerical method. The linear case of $C_2 = 0$ with real-valued C_0 and C_1 has been previously validated and compared with other methods [16,17]. We therefore confine ourselves to demonstrating convergence for a single plate, with both a linear example (with complex-valued C_1 and $C_2 = 0$) and a non-linear example, as well as a simple multiple plate example. We take $M = N$ throughout. Comparison with experimental data and high-fidelity numerics is provided in Section 5, and in this section, we focus on numerical convergence as opposed to a specific physical model or findings. We compute the relative error of P (given by (3.4)), as well as the relative error of $[p]$ along the plate (measured in the L^2 norm using a large number of discrete points), by comparing to a larger value of $M = N$. We tested the numerical method extensively, and for all cases, we found similar behaviour to the two following examples.

4.1. Interrogation for a single plate

To demonstrate generality (similar convergence also occurred for the experiments in Section 5), we consider the case of

$$C_0(x) = k_0^2, \quad C_1(x) = \mathrm{i}k_0(1.2 + \sin(20x)), \quad C_2(x) = \mathrm{i}20k_0^2(x^2 + 1),$$

where C_2 is set to zero for the linear case. The pressure due to the acoustic source is taken to be a plane wave of unit amplitude incident at angle $\pi/3$, as in (2.1).

Fig. 2 shows the convergence for $k_0 = 5$ and $k_0 = 100$. We see that in both cases we can obtain a relative accuracy of at least 10^{-7} for $[p]$ and 10^{-10} for P, for $M = N = 1000$. We also see that, for a given accuracy, a smaller number of basis functions are needed for a smaller k_0. Consistent with the linear case in previous works, there is a value of $M = N$ (typically of the order k_0) after which the convergence rate increases (particularly visible in the P error curves), before settling to an algebraic rate for large $M = N$.[2] Fig. 3 shows the corresponding far-field directivities. The non-linear term causes an amplification of the scattered sound, though the scattered field still concentrates around the expected lobes, particularly for larger k_0.

Finally, we consider the convergence of iterates of Newton's method. For a fixed k_0 and fixed $M = N$, we consider the convergence of the iterates to the vector of coefficients $\{\tilde{a}_m\}_{m=1}^{M}$ in $\mathbb{C}^M$, taking the relative l^2-norm error of the computed

[1] There is an additional reason for choosing the linearised solution as the initial vector. We cannot rule out the possibility of multiple solutions to the non-linear system of Eq. (3.10). In the case of multiple solutions, we expect the physically correct solution to be the one closest to the linearised solution. However, in the following examples we checked for additional solutions using deflation and were unable to find any. This provides numerical evidence (though not a mathematical proof) that there is a unique solution to (3.10). For further details on Newton's method and deflation in the context of spectral methods and infinite-dimensional problems, see, for example, the thesis of Birkisson [27] and the references therein.

[2] For the case of a rigid impermeable plate with the usual linear boundary conditions, i.e. $C_0 = 0$, this convergence is improved to exponential. This is because, in this case, the sine functions (used in Section 3.2) in elliptic coordinates, and more specifically, the sine-elliptic functions correctly capture the square-root type behaviour of $[p]$ at the ends of the plate.

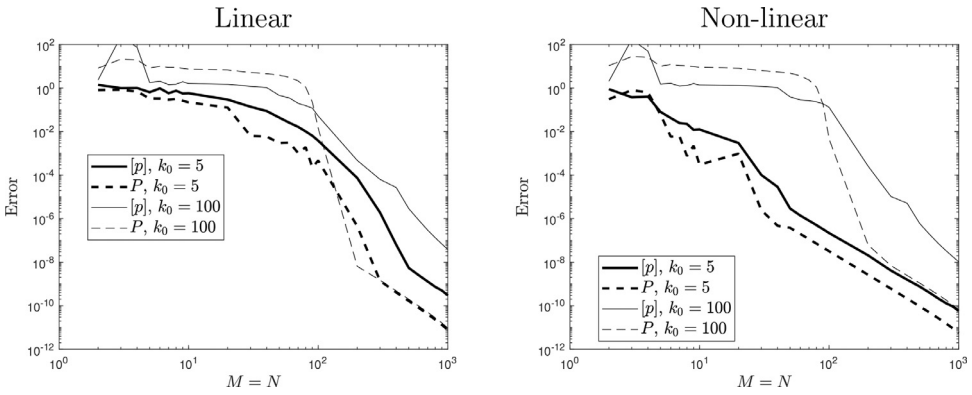

Fig. 2. Convergence of the method for the linear case (left) and non-linear case (right).

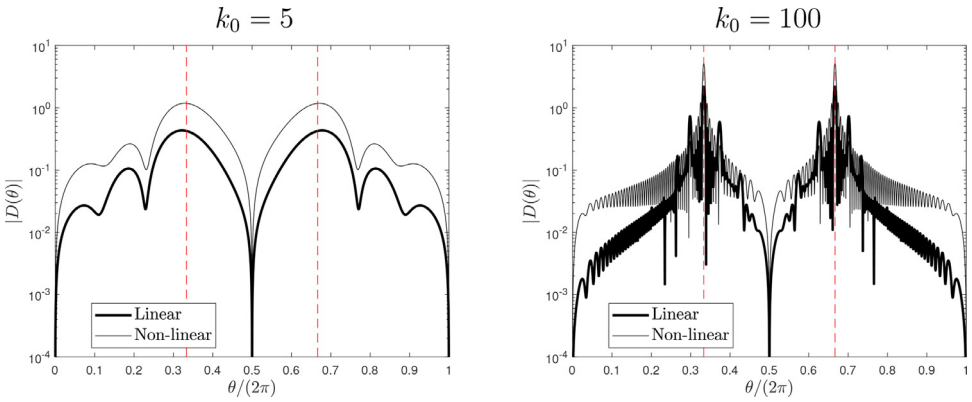

Fig. 3. Far-field directivities; the dotted lines show the positions of the expected dominant lobes.

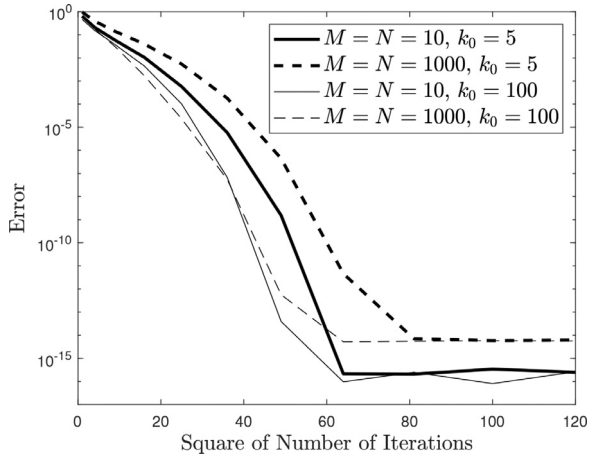

Fig. 4. Convergence of Newton's method to solve the non-linear equation in (3.10). We have plotted the relative error of the sought after coefficients $\tilde{a}_m$ (convergence for the $\tilde{b}_j$ is similar), which are computed from the solution of (3.10) by solving the linear Eq. (3.9).

coefficients. Note that we measure the error relative to the converged (in terms of the Newton iterates) values of $\{\tilde{a}_m\}_{m=1}^{M}$ for a fixed $M = N$, rather than compared to the actual coefficients a_m. This allows us to see how fast Newton's method converges for the truncated/discretised Eq. (3.8). Fig. 4 shows the results, where we have plotted the square of the number of iterations of Newton's method along the horizontal axis. This scaling shows the expected quadratic convergence (i.e. the number of correct digits roughly doubles each iteration). There are two further notable features. First, as expected, a larger $M = N$ requires a larger number of iterations and also has a larger error plateau. However, the number of iterations to gain near machine precision is still very small for all the parameter values we consider throughout this paper (we never

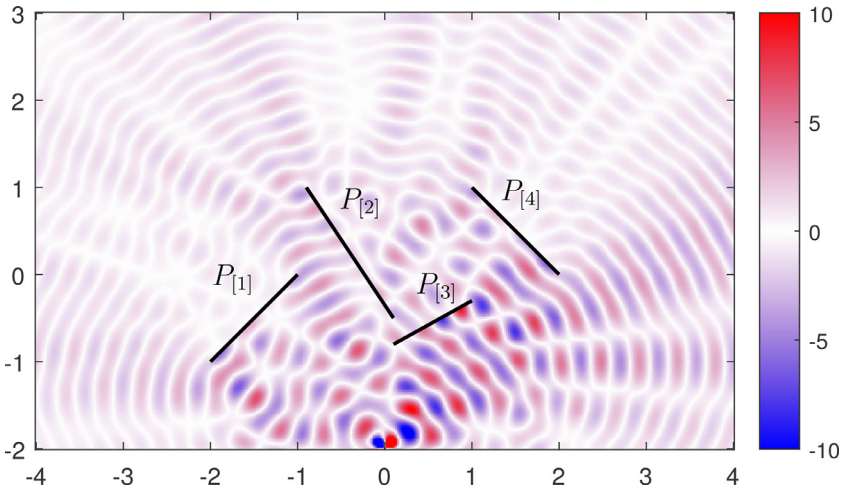

Fig. 5. Real part of total field for multiple plate example.

needed more than ten iterations and did not run into any convergence issues). Second, it appears that one or two fewer iterations are needed for $k_0 = 100$ compared to $k_0 = 5$. We found that the number of iterations needed varies weakly with k_0. For $k_0 \geq 1$, this is due to the scalings in the coefficients of C_0, C_1, C_2 in terms of k_0. Using the standard error analysis of Newton's method near a solution (in terms of the Jacobian and higher-order derivatives), it is easy to construct examples of different scalings where the number of iterations needed increases or decreases with increasing k_0. Hence, and because only a small number of iterations are needed for the selected parameters in this paper, we have not pursued the (difficult) task of a general analysis of the number of iterations needed in terms of k_0 and $M = N$. Instead, we terminate the iteration process when the residual of the non-linear system is near machine precision.

4.2. Interrogation for multiple plates

To demonstrate the method for four plates, we consider the parameters

$$C_0^{[1]}(x_{[1]}) = k_0^2, \qquad C_1^{[1]}(x_{[1]}) = \mathrm{i}k_0, \qquad C_2^{[1]}(x_{[1]}) = 30\mathrm{i}k_0^2,$$
$$C_0^{[2]}(x_{[2]}) = 0,$$
$$C_0^{[3]}(x_{[3]}) = 1, \qquad C_1^{[3]}(x_{[3]}) = \tanh(x_{[3]}), \qquad C_2^{[3]}(x_{[3]}) = -\sin(\pi x_{[3]})$$
$$C_0^{[4]}(x_{[4]}) = -1, \qquad C_1^{[4]}(x_{[4]}) = 1/\cosh(x_{[4]}), \qquad C_2^{[4]}(x_{[4]}) = \mathrm{i}\sqrt{|x_{[4]}|}.$$

Again, these parameters are not chosen to correspond to any specific physical model (though the parameters for the first plate can be cast in terms of the physical model of this paper), but rather to demonstrate the generality of the method and the ability to cope with both a range of functions and a mixture of sign patterns. This flexibility exhibits the versatility commonly found in collocation approaches. We leave the investigation of physical models with multiple plates for future work. In defining the above parameters, we have not specified $C_1^{[2]}$ and $C_2^{[2]}$ since the second plate is rigid and impermeable.

We consider the case of $k_0 = 15$ and a quadrupole sound source at $(0, -2)$ with $P_0 = 1$ in (2.2). The four plates and total field are shown in Fig. 5. Convergence of the method for this example is shown in Fig. 6, where we see the same behaviour as before (here, we set $M_{[i]} = M$ and $N_{[i]} = N$). In this example, all relative errors are well below 10^{-6} for $M = N = 100$. We also show the far-field directivity in Fig. 6 (right), which shows a complicated structure due to interference of scattered fields from multiple sharp edges in similar proximity to the source.

5. Results

5.1. Comparison to LES

First we attempt to verify our results with the existing LES results for porous plates which take into account the Forchheimer correction [12,13]. In particular, we recreate the directivity patterns from [13, Fig. 29]. In that paper, a plate of uniform thickness of $h = 3$ mm and total chord length 10 cm is simulated in a uniform flow of 20 ms^{-1}. The fore-region of the plate is impermeable (solid) and the aft-region is porous, with a permeability coefficient

$$K = \frac{d_p^2 \phi^3}{C_K (1-\phi)^2}, \tag{5.1}$$

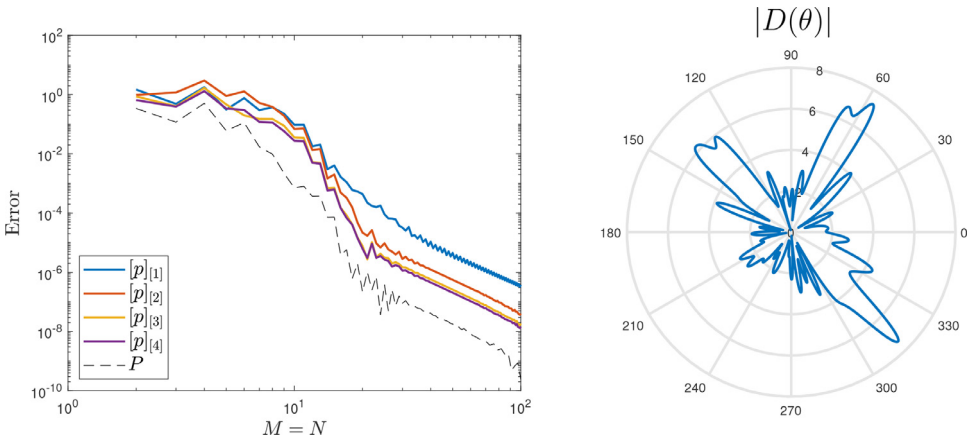

Fig. 6. Left: Convergence for multiple plate example. Right: far-field directivity $|D(\theta)|$.

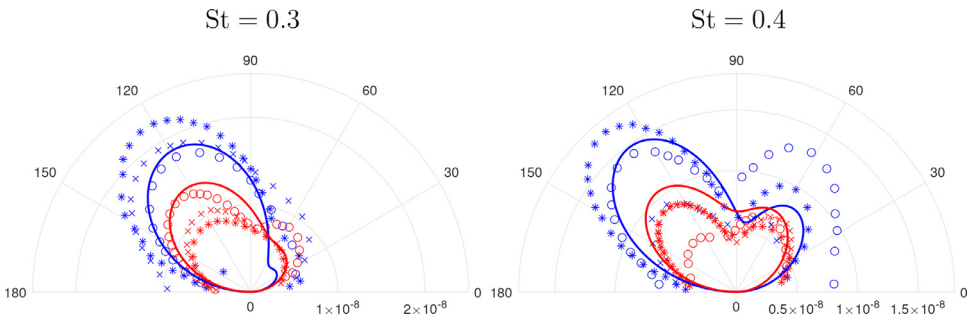

Fig. 7. Far-field directivity plots comparing data from [13, Fig. 30] (symbols) to our model predictions. Blue corresponds to the impermeable/solid cases, and red to the porous cases. The symbols correspond to Cases A (∗), B (○) and C (×). (For interpretation of the references to colour in this figure legend, the reader is referred to the web version of this article.)

and a Forchheimer coefficient

$$F = \frac{d_p \rho}{C_F(1-\phi)\mu}|v|. \tag{5.2}$$

Here, $\phi = 0.5$ is the porosity parameter, and $d_p = 0.078$ mm denotes the typical particle diameter. The coefficients are $C_K = 180$ and $C_F = 100$.[3] These parameters correspond to $K = 1.7 \times 10^{-11}$ and $\beta = 0.38$ in our model definitions, and we use the non-dimensional thickness $h = 0.03$.[4]

For comparison, we include all edge shapes from [13]; rounded edges (Case A), square/sharp edges (Case B, which our setup most accurately mimics), and fully circular edges (Case C). We have extracted the data from [13, Fig. 30] and replotted with predictions from our model for a quadrupole at (1,0.05) in flow of $M = 0.06$ in Fig. 7. Vortex shedding occurs at $\mathrm{St} \approx 0.2$ which is neglected in our model, thus we only consider the data for $\mathrm{St} = 0.3, 0.4$. The quadrupole model results have been rescaled by 9×10^{-7} and 6.75×10^{-7} respectively to align with the results from [13]. We have rescaled since the results in Koh et al. [13, Eq. (23)] use parameters which are not present in our model, such as spanwise correlation lengthscales and a finite plate span. However, since these are multiplicative factors to the overall power spectral density, the relative noise reduction should be well captured by our model (as these factors cancel out when we take logarithms to calculate the noise in dB).

The results in Fig. 7 indeed compare well and indicate that our model is capable of rapidly evaluating the effects of a non-linear Forchheimer boundary condition on trailing edge noise generated by porous aerofoils (producing all of our data for each plot in Fig. 7 took less than a tenth of second on a six year-old laptop). As expected, there are some discrepancies since LES allow for fully turbulent flows, in particular, multiple turbulent eddies and therefore a streamwise correlation

[3] The dimensional parameter d_p is found by calculating the inner wall lengthcale, $l^* = \nu/u_\tau$ from the boundary-layer based Reynolds number $\mathrm{Re}_\tau = \delta_{99}/l* = 492$ where δ_{99} is the 99% boundary layer thickness, equal to $1.5h$, and combining with the stated $\mathrm{Re}_K = \sqrt{K}/l* = 0.45$.

[4] This is chosen since Koh's model uses a volume averaging over the fluid inside the porous material, $< \cdot >^\gamma$, rather than, as we have defined, the average over the total volume (including both solid and fluid phases). To avoid needing to alter our dimensional definitions of μ and ρ_f in (1.2), it is easiest to adapt our model to match Koh's boundary condition [13, Eq. (2)] by scaling h by $1/\phi$ since $\mu = \phi < \mu >^\gamma$ and $\rho_f = \phi < \rho_f >^\gamma$.

Table 1
Summary of test cases. †No inertial parameter specified; we have selected an inertial parameter close to that of the sintered material of Case 4.

Case	K (m^2)	β	Material	Ref.
1	0	–	Impermeable	–
2	2.7×10^{-9}	0.14	Alantum NiCrAl open-cell metal foam	[9]
3	5.72×10^{-11}	0.5†	Sintered PE granulate (Porex)	[28]
4	3.65×10^{-12}	0.613	Sintered SUS316L powder (Group 2, 9 mm)	[29]

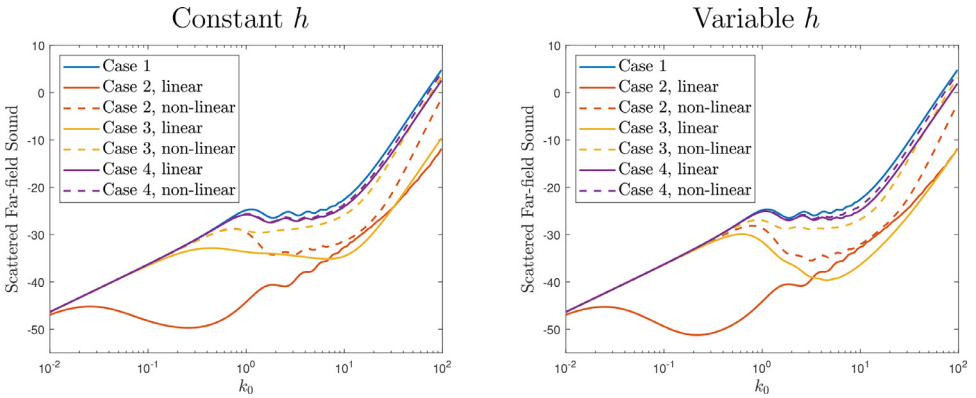

Fig. 8. Far-field sound across a range of frequencies for each Case. Left: Results for non-dimensionalised thickness of $h(x) = 0.012$. Right: Results for an NACA 4-digit aerofoil with 6% thickness.

lengthscale. Further, it is possible that the spanwise correlation lengthscale varies between porous and impermeable cases which we cannot account for.

5.2. Comparison to experiments

We now present a selection of results for various porous materials that have been used in experimental tests. For these we first determine their porous properties, namely the permeability K and Forchheimer coefficient β. The remaining parameters shall be set as standard for air: $\rho = 1.225\,\mathrm{kg\,m^{-3}}$, $c_0 = 343\,\mathrm{ms^{-1}}$, $\mu = 1.81 \times 10^{-5}\,\mathrm{Pa\,s}$, and we shall use a semichord length of 75 mm which is in line with small-scale experimental wind tunnel tests [1,4,9,28]. We obtain a number of test case parameters for K and β from [9,28,29], which are summarised in Table 1.

First, we compare the linear and non-linear prediction for noise generated by a quadrupole close to the trailing edge of a plate of uniform thickness of 0.9 mm corresponding to a non-dimensionalised thickness of $h(x) = 0.012$. This thickness is much larger than the characteristic size of the selected materials in Table 1, which vary from $\sim 50 - 800$ µm. The quadrupole is placed at (0.99,0.1), corresponding to a vertical height of 5% chordlength. When considering Case 2, we alter C_0 to

$$C_0(x) = \begin{cases} 0, & \text{if } x \leq 0.6, \\ k_0^2, & \text{otherwise,} \end{cases}$$

in order to more accurately model the setup of [9] (here x corresponds to the parametrisation of the plate lying in $\{(x, 0) : -1 \leq x \leq 1\}$). There, an impermeable aerofoil had porous inserts appended to the trailing edge, resulting in potential junction noise (at the impermeable-permeable junction). This choice of C_0 endows our model with similar properties; an impermeable fore section, $-1 < x \leq 0.6$, and a porous rear section, $0.6 < x < 1$.

Fig. 8 (left) illustrates the non-dimensional scattered far-field sound, defined in (3.4) as $10 \log_{10} \int_0^{2\pi} |D(\theta)|^2 d\theta$, for our four cases. Case 1 is the reference impermeable case. We see that for low permeability (Case 4) there is little difference between the linear and non-linear predictions over the whole frequency range, and such a low permeability does not produce a significant noise reduction versus the impermeable Case 1. As permeability increases, the noise reduction versus the impermeable plate increases but so too does the difference between the linear and non-linear results for mid and high frequencies. Thus, for higher permeability, inertial effects can become significant on the generation of aerodynamic noise. The particular metal foam for Case 2 has the largest pores ~ 800 µm, thus the largest local Reynolds number. It is therefore expected that the non-linear effects should be greatest in this case [10].

The maximum noise reduction observed by Rubio Carpio et al. [9] for Case 2 was 10 dB, and a noise increase of ~ 8 dB was observed at high frequencies. The linear prediction hugely overestimates the noise reduction and does not capture any possible noise increase, whereas the non-linear model predicts a similar ~ 10 dB noise reduction. As frequency increases, the noise reduction does diminish for the non-linear case, although an increase is not seen. The high-frequency noise increase

in the results of [9] is dominated by roughness noise. Hence, we do not expect to capture this feature in our model. Furthermore, for this case, the local Reynolds number is $\mathrm{Re}_L \sim 54\omega\eta_a$, where $\omega\eta_a$ is the local flow speed. This highly porous material constructed from large cells may therefore exceed the limit of validity of the Forchheimer model ($1 < \mathrm{Re}_L < 10$, [10]). Nevertheless, the results indicate a reasonable comparison to [9].

Case 3 has a lower local Reynolds number than Case 2 due to smaller pore sizes and thus should be better described by the Forchheimer model. The acoustic results from Geyer et al. [28] for Case 3 indicate a maximum noise reduction of ~ 6 dB, and a noise increase at higher frequencies. Our non-linear model again captures a similar maximum noise reduction, and trends towards a noise increase at high frequencies. Of course, this model still excludes any surface roughness noise, which becomes important at high frequencies. However, we can see that not all of the noise increase at high frequencies can be directly attributed to surface roughness, and some should be attributed to inertial (non-linear) effects. The noise increase observed in Geyer et al.'s data [28, Fig. 6 bottom panel] at low frequencies is a spectral peak that is attributed to trailing-edge bluntness noise which is not captured in our model. Thus we do not observe a similar peak in our results.

Case 4 has the lowest local Reynolds number and lowest permeability. Thus the effects of inertia should be weakest. Indeed this is observed in our results since the linear and non-linear predictions differ only by ~ 1 dB. The defined porosity of the material in Case 4 is close to 50% (Cases 2 and 3 have higher porosities). Therefore, we anticipate that for materials with porosities lower than $\sim 50\%$, the linear Darcy model would be suitable. However, for materials with greater porosities, the non-linear inertial effects must be included. Predictions from this model, however, will only be accurate if the local Reynolds number is sufficiently small $\mathrm{Re}_L < 10$, thus materials with large open pores may still not be suitably described. We repeat the results for a NACA 4-digit aerofoil with 6% thickness in Fig. 8 (right), and, as expected, observe similar trends to the constant thickness plate case.

To investigate further the agreement with experimental results and the impact the location of the quadrupole source, we plot the noise reduction in Fig. 9 for Case 2 and Case 3. Here, a positive value indicates that the corresponding case is quieter than a fully impermeable plate of the same geometry by that many dB. We include a range of quadrupole locations at $(1, 0.1), (1, 0.05), (0.97, 0.09), (0.99, 0.06)$ corresponding to heights of 3.3–7.05 mm above the surface of the plate. Since all quadrupole sources are scaled as required by Lighthill's analogy [18], we see only a minor impact due to the location of the point quadrupole. Both Case 2 and Case 3 illustrate that the plate geometry has a minor effect on noise reduction for the non-linear case, but a more significant effect in just the linear case. Data from [28] in Fig. 10 for Case 3 covers a wider range of comparable frequencies and, discounting the trailing-edge bluntness noise increase ($k_0 \sim 4$), and high-frequency roughness noise ($k_0 \gtrsim 20$) we see reasonable agreement between the non-linear model and the experimental results. Here our model uses the sum of all four quadrupoles as its acoustic source. The linear model in contrast (with the same source) greatly over predicts the noise reduction. Whilst we do not expect our quadrupole model to replicate a fully turbulent trailing-edge flow, we see that, with appropriate Lighthill scaling, the non-linear model is replicating realistic noise reductions whereas the purely linear model is not.

5.3. Far-field directivity and surface pressure distribution

Finally, we consider the effect of the non-linear boundary condition on the far-field directivity and surface pressure jump at specific frequencies to interrogate the physical effects of introducing this non-linear correction. We focus specifically on Case 3 for which we know the Forchheimer model is well-suited. Fig. 11 illustrates the pressure jump across $y = 0$ for both linear and non-linear boundary conditions for a plate of constant thickness, alongside the far-field directivity (plotted on a log scale). For low frequencies ($k_0 = 0.1$), there is little difference between the linear and non-linear results, and thus minimal impact of inertia, as is expected due to relatively low velocities. For higher frequencies and thus higher velocities, we see the non-linear results produce a higher trailing-edge peak surface pressure than the linear case, indicating that whilst viscosity dissipates pressure at the surface, inertial effects either hinder this viscous mechanism or independently amplify pressure. The effect of this difference in surface pressure on the far-field directivity is twofold. First, a higher overall surface pressure for the non-linear case results in a greater overall magnitude of far-field noise. Second, a higher peak trailing-edge pressure for the non-linear case results in a scattered field dominated by just the scattering at the trailing edge, and thus a reduced interference pattern in the far-field directivity when compared to the linear case (fewer oscillations).

These results are repeated for the NACA 0006 profile in Fig. 12, where overall similar effects are observed for $k_0 = 0.1, 1$. The variable thickness plate, however, results in a more oscillatory surface pressure at high frequencies ($k_0 = 10$) than the constant thickness plate. The impact of this is an increased interference-type pattern (more oscillations) in far-field directivities, with the linear case being most impacted upon comparison to Fig. 11. Nevertheless, inertial effects in the non-linear model again govern the amplitude of the overall surface response, and as for the constant-thickness case, the trailing-edge peak is far more dominant in the non-linear case than in the linear case. Therefore, despite some impact from the viscous effects on the far-field directivity, overall the dominance of the trailing-edge peak for the non-linear model determines the total scattered noise and thus there is minimal difference between the constant and variable thickness plates observed in Fig. 9 (right).

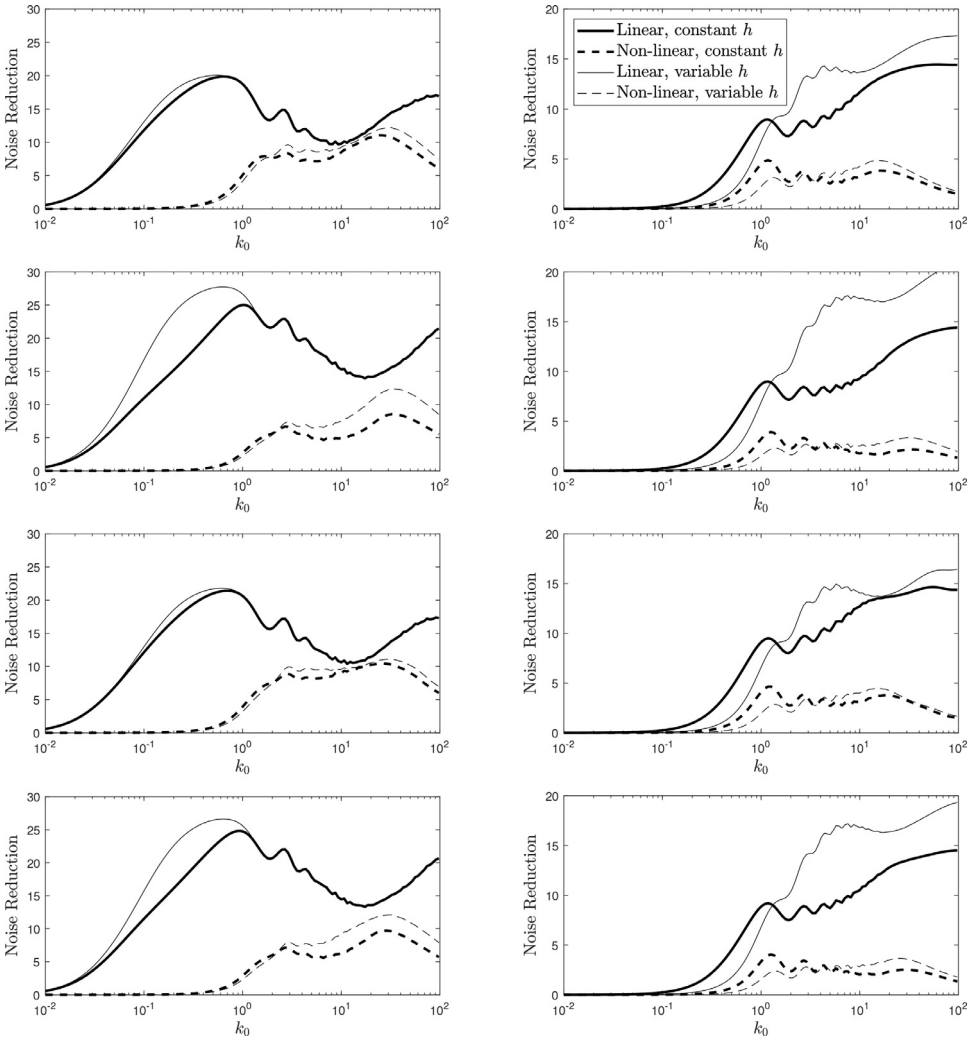

Fig. 9. Noise reduction calculated for Cases 2 (left) and 3 (right) for various quadrupole sources (locations 1–4 from top to bottom).

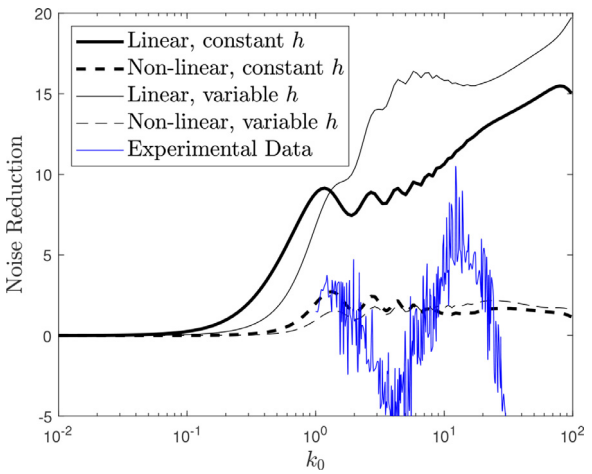

Fig. 10. Comparison of noise reduction for multiple quadrupole sources with experimental data from [28, Fig. 6 bottom panel].

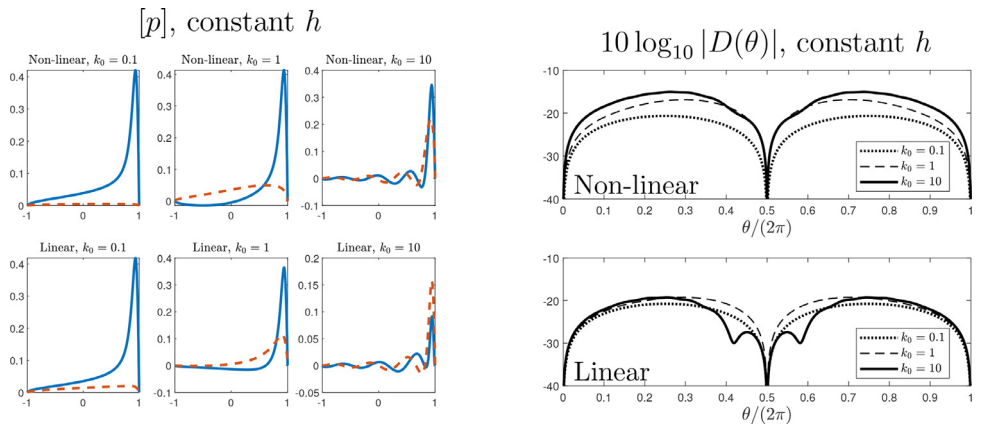

Fig. 11. Left: Surface pressure jump for different values of k_0. The real parts are shown as solid lines, whereas the imaginary parts are shown as dashed lines. Right: Far-field (log) directivity. In all cases, the plate thickness is constant, $h = 0.012$.

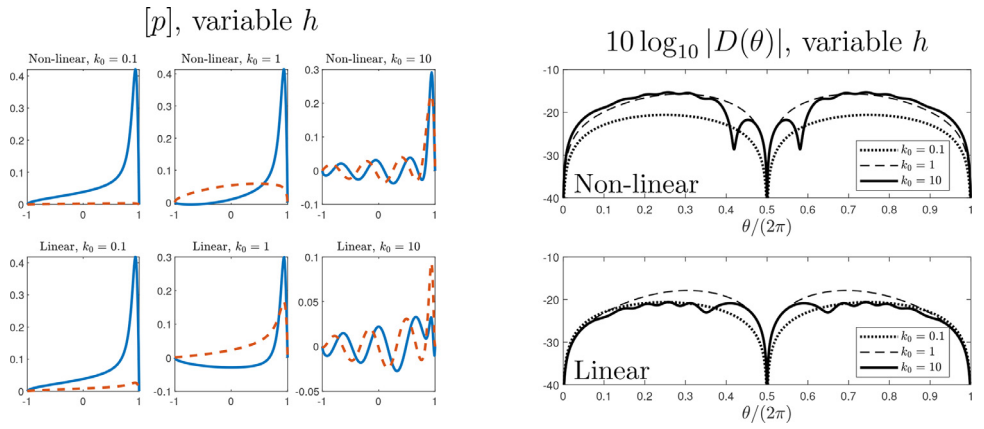

Fig. 12. Left: Surface pressure jump for different values of k_0. The real parts are shown as solid lines, whereas the imaginary parts are shown as dashed lines. Right: Far-field (log) directivity. In all cases the plate thickness takes a NACA 0006 profile.

6. Conclusion

This paper has presented a low-fidelity numerical solution to rapidly predict aerofoil trailing-edge noise accounting for both linear viscous effects and non-linear inertial effects within metal foam-like porous materials. The linear model at high frequencies can hugely over-predict the noise reduction upon comparison with experimental data. However, when supplemented with a non-linear Forchheimer correction, we see good agreement in maximum noise reduction predictions versus experimental data. The model can account for constant or non-constant plate thickness, however, for quadrupole-type noise sources, the peak scattered pressure on the surface at the trailing edge is sufficiently dominant that the effects of altering the aft (front) of the plate are minimal. Conversely, if only viscous (linear) effects are accounted for, significant attenuation of the source occurs at the trailing edge, and therefore the response along the full plate contributes to the far-field scattered noise; variations in the boundary conditions along the plate, therefore, have a greater impact on the scattered noise.

We conclude that for mid and high frequencies and typical high permeability materials, the local inertial effects at the trailing edge can dominate the overall acoustic scattering behaviour. Thus accurate modelling of the aft of the aerofoil is unnecessary in comparison to the importance of including the inertial effects of the material local to the source, in this case, the boundary layer. Of course, it is not solely the permeability which determines the inertial effects, since an independent inertial coefficient in the Forchheimer model must also be provided to characterise the porous material. It may also be the case that this inertial coefficient is non-constant; many empirical formulae exist for permeable rocks [30]. However, the literature is less complete for the application considered here of metal foams in air. Since the model presented here can deal with non-constant coefficients, a variable Forchheimer coefficient or indeed a chord-wise variable permeability coefficient could certainly be used should one be determined for a material of interest, or wish to consider partially porous aerofoils. This model further does not account for the impact of the rough porous surface on the generation of turbulence, and cannot capture any roughness noise measured experimentally. However, it may be possible to supplement this model with a prediction of surface roughness noise [31].

Regarding the numerical method, future work will look at the possible inclusion of hierarchical solvers for multiple plates and methods for the rapid evaluation of the solution at a large number of points. One further possibility when solving by iteration, in the case of multiple plates, is to split up the non-linear relation according to the plates to reduce the size of the linear systems. Finally, spectral methods such as those in this paper have great flexibility in terms of the possible boundary conditions and different models that can be numerically solved. We hope that this will be useful for further problems in addition to the current paper.

Numerical code

Downloadable code (written in MATLAB) for the method of this paper is provided at https://github.com/MColbrook/MathieuFunctionCollocation.

Author contributions

M.J.C. developed the numerical method and analysed its performance. Both authors developed the examples and contributed to the writing of the manuscript.

Declaration of Competing Interest

The authors declare that they have no known competing financial interests or personal relationships that could have appeared to influence the work reported in this paper.

Acknowledgements

This work was supported by EPSRC grant EP/L016516/1 and a Research Fellowship at Trinity College, Cambridge (M.J.C.) and an EPSRC Early-Career Fellowship EP/P015980/1 (L.J.A.). M.J.C. would like to thank Alex Townsend and Andrew Horning for discussions regarding the method of this paper, and L.J.A is most grateful to Ankit Rohatgi, creator of WebPlotDigitizer, for the ability to extract data from the literature. The authors would also like to extend their thanks to Justin Jaworski for his assistance in determining the porous boundary conditions.

Supplementary material

Supplementary material associated with this article can be found, in the online version, at doi:10.1016/j.jsv.2020.115905.

References

[1] T. Geyer, E. Sarradj, C. Fritzsche, Measurement of the noise generation at the trailing edge of porous airfoils, Exp. Fluids 48 (2010) 291–308, doi:10.1007/s00348-009-0739-x.
[2] E. Sarradj, T. Geyer, Symbolic regression modeling of noise generation at porous airfoils, J. Sound Vib. 333 (14) (2014) 3189–3202, doi:10.1016/j.jsv.2014.02.037.
[3] T. Geyer, E. Sarradj, C. Fritzsche, Porous airfoils: noise reduction and boundary layer effects, Int. J. Aeroacoust. 9 (6) (2010) 787–820, doi:10.1260/1475-472X.9.6.787.
[4] P. Chaitanya, P. Joseph, T. Chong, M. Priddin, L. Ayton, On the noise reduction mechanisms of porous aerofoil leading edges, J. Sound Vib. 485 (2020) 115574, doi:10.1016/j.jsv.2020.115574.
[5] J. Jaworski, N. Peake, Aerodynamic noise from a poroelastic edge with implications for the silent flight of owls, J. Fluid Mech. 723 (2013) 456–479, doi:10.1017/jfm.2013.139.
[6] L. Rayleigh, The Theory of Sound, 2, Dover, 1945.
[7] M. Howe, M. Scott, S. Sipcic, The influence of tangential mean flow on the Rayleigh conductivity of an aperture, Proc. Roy. Soc. A 452 (1953) (1996) 2303–2317, doi:10.1098/rspa.1996.0123.
[8] M. Howe, M. Lighthill, On the theory of unsteady high Reynolds number flow through a circular aperture, Proc. R. Soc. Lond. A 366 (1725) (1979) 205–223, doi:10.1098/rspa.1979.0048.
[9] A. Rubio Carpio, F. Avallone, D. Ragni, M. Snellen, S. van der Zwaag, Mechanisms of broadband noise generation on metal foam edges, Phys. Fluids 31 (10) (2019) 105110, doi:10.1063/1.5121248.
[10] F. Cimolin, M. Discacciati, Navier–Stokes/Forchheimer models for filtration through porous media, Appl. Numer. Math. 72 (2013) 205–224, doi:10.1016/j.apnum.2013.07.001.
[11] L. Ayton, M. Colbrook, T. Geyer, P. Chaitanya, E. Sarradj, Reducing aerofoil–turbulence interaction noise through chordwise-varying porosity, J. Fluid Mech. 906 (2020), doi:10.1017/jfm.2020.746.
[12] S. Koh, B. Zhou, M. Meinke, N. Gauger, W. Schröder, Numerical analysis of the impact of variable porosity on trailing-edge noise, Comput. Fluids 167 (2018) 66–81, doi:10.1016/j.compfluid.2018.02.015.
[13] S. Koh, M. Meinke, W. Schröder, Numerical analysis of the impact of permeability on trailing-edge noise, J. Sound Vib. 421 (2018) 348–376, doi:10.1016/j.jsv.2018.02.017.
[14] Y. Bae, Y. Moon, Effect of passive porous surface on the trailing-edge noise, Phys. Fluids 23 (12) (2011) 126101, doi:10.1063/1.3662447.
[15] V. Ananthan, P. Bernicke, R. Akkermans, T. Hu, P. Liu, Effect of porous material on trailing edge sound sources of a lifting airfoil by zonal overset-LES, J. Sound Vib. 480 (2020) 115386, doi:10.1016/j.jsv.2020.115386.
[16] M. Colbrook, M. Priddin, Fast and spectrally accurate numerical methods for perforated screens (with applications to Robin boundary conditions), IMA J. Appl. Math. 85 (5) (2020) 790–821, doi:10.1093/imamat/hxaa021.
[17] M. Colbrook, A. Kisil, A Mathieu function boundary spectral method for scattering by multiple variable poro-elastic plates, with applications to metamaterials and acoustics, Proc. R. Soc. A 476 (2241) (2020) 1–21, doi:10.1098/rspa.2020.0184.
[18] M. Lighthill, On sound generated aerodynamically I. General theory, Proc. R. Soc. Lond. A 211 (1107) (1952) 564–587, doi:10.1098/rspa.1952.0060.

[19] P. Morse, P. Rubenstein, The diffraction of waves by ribbons and by slits, Phys. Rev. 54 (11) (1938) 895.
[20] D. Nigro, Prediction of broadband aero and hydrodynamic noise: derivation of analytical models for low frequency, The University of Manchester (United Kingdom), 2017 Ph.D. thesis.
[21] M. Colbrook, L. Ayton, A. Fokas, The unified transform for mixed boundary condition problems in unbounded domains, Proc. R. Soc. A 475 (2222) (2019) 1–21, doi:10.1098/rspa.2018.0605.
[22] L. Ayton, M. Colbrook, A. Fokas, The unified transform: a spectral collocation method for acoustic scattering, in: 25th AIAA/CEAS Aeroacoustics Conference, 2019, p. 2528.
[23] N. McLachlan, Theory and Application of Mathieu Functions, Clarendon Press, 1951.
[24] F. Olver, D. Lozier, R. Boisvert, C. Clark, NIST Handbook of Mathematical Functions, Cambridge University Press, 2010.
[25] J. Boyd, Chebyshev and Fourier Spectral Methods, Courier Corporation, 2001.
[26] L. Trefethen, Spectral Methods in MATLAB, 10, Siam, 2000.
[27] Á. Birkisson, Numerical solution of nonlinear boundary value problems for ordinary differential equations in the continuous framework, University of Oxford, 2013 Ph.D. thesis.
[28] T. Geyer, E. Sarradj, Trailing edge noise of partially porous airfoils, in: 20th AIAA/CEAS Aeroacoustics Conference, 2014, p. 3039.
[29] W. Zhong, X. Ji, C. Li, J. Fang, F. Liu, Determination of permeability and inertial coefficients of sintered metal porous media using an isothermal chamber, Appl. Sci. 8 (9) (2018), doi:10.3390/app8091670.
[30] D. Takhanov, Forchheimer model for non-Darcy flow in porous media and fractures, Imperial College London, 2011 MSc thesis.
[31] L. Ayton, Bioinspired aerofoil adaptations: the next steps for theoretical models, Philos. Trans. R. Soc. A 377 (2159) (2019) 20190070, doi:10.1098/rsta.2019.0070.